JACS
JOURNAL OF THE AMERICAN CHEMICAL SOCIETY
pubs.acs.org/JACS

Article

Temperature Dependence of the Hydrated Electron's *g*-Factor and Persistence of a Cavity-Localized Electron at Elevated Temperature

Ar. M. Fonlon, Christopher J. Mundy, and John M. Herbert*

Cite This: *J. Am. Chem. Soc.* 2026, 148, 36675−36686

Read Online

ACCESS | Metrics & More | Article Recommendations | Supporting Information

ABSTRACT: The structure of the aqueous electron, e^-(aq), has been the focus of intense scrutiny from both theory and experiment. The temperature dependence of its *g*-factor, measured via electron paramagnetic resonance and shifted significantly from the free-electron value, has been suggested to be inconsistent with the conventional picture of an electron localized in a solvent void or "cavity". Here, we use *ab initio* molecular dynamics simulations and quantum chemistry calculations to compute the ensemble-averaged, isotropic *g*-factor for e^-(aq) over the entire temperature range of liquid water. A temperature-dependent shift is obtained, in reasonable agreement with experiment, without any qualitative change in either the localized structure of e^-(aq) or its average coordination number. Far from being inconsistent with *g*-factor measurements, persistence of the cavity motif actually supports the rather mild temperature dependence of the *g*-factor because the amount of spin density hosted in oxygen orbitals is remarkably insensitive to temperature. These results support a cavity-localized picture of e^-(aq) from 0−100 °C at atmospheric pressure. The simulations are also broadly consistent with spectroscopic measurements demonstrating that the molar extinction coefficient is insensitive to temperature and that there are no abrupt temperature-induced changes in the absorption spectrum, even into the supercooled and supercritical water regimes. This analysis further entrenches the cavity-centric picture of e^-(aq).

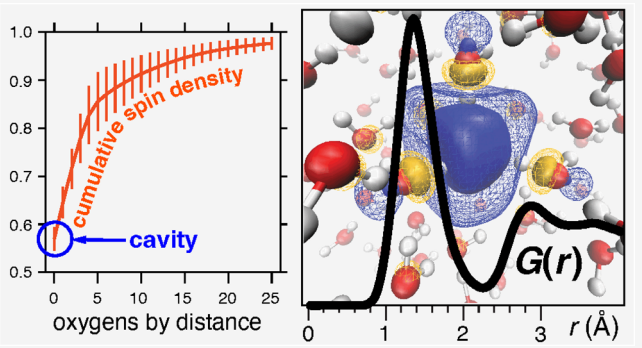

1. INTRODUCTION

The hydrated electron, e^-(aq), is the primary reducing agent in the radiation chemistry of aqueous systems.[1−5] Structurally, it forms hydrogen bonds to water molecules like any other anion,[5−10] yet its mass makes it a fundamentally quantum-mechanical solute (Figure 1). Its structure has been debated at length and a consensus has emerged around a semilocalized charge defect inhabiting a void in the structure of liquid water,[6] albeit with 40−50% of the spin density penetrating beyond this excluded volume.[8−11] This cavity-centric picture is supported by numerous *ab initio* calculations,[10−27] and by experiments,[28−34] with interpretation of the latter often aided by simulation.[29−33]

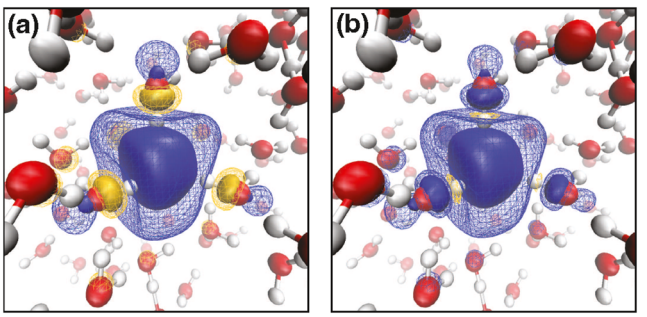

Figure 1. Snapshot from an *ab initio* MD simulation of e^-(aq) at T = 300 K, illustrating (a) the SOMO and (b) the spin density. Opaque and wire mesh surfaces encapsulate 50% and 80%, respectively, of the probability density and the blue and gold isosurfaces indicate the sign change that occurs atop the water molecules that coordinate directly to the unpaired electron.

Already in the 1960s, electron paramagnetic resonance (EPR) experiments established that e^-(aq) is a localized species, coordinated to water molecules rather than delocalized over a large number of them.[35,36] This picture was later refined to include charge penetration beyond the excluded volume or cavity, based on electron spin-echo experiments in low-temperature glassy matrices.[37−40] Those experiments and others provided some evidence for a coordination number of n = 6 in γ-irradiated glasses,[36,38−43] although hyperfine spectra

Received: April 4, 2026
Revised: August 17, 2026
Accepted: August 18, 2026
Published: August 24, 2026

https://doi.org/10.1021/jacs.6c07020
J. Am. Chem. Soc. 2026, 148, 36675−36686

may not be sufficient to characterize the coordination number unambiguously.[44,45]

The hyperfine spectra are consistent with a node in the electron's wave function that is located near the hydrogen atoms that coordinate to the unpaired electron.[43] In quantum chemistry calculations of e^-(aq), a node in the singly occupied molecular orbital (SOMO) is always evident because the SOMO must be orthogonal to the MOs of the water molecules (Figure 1a).[6] A node is also evident in the spin density

$$\rho_{\text{spin}}(\mathbf{r}) = \rho_{\alpha}(\mathbf{r}) - \rho_{\beta}(\mathbf{r}) \quad (1)$$

that is depicted in Figure 1b and is largely indistinguishable from the SOMO. *Ab initio* molecular dynamics (MD) simulations suggest that the SOMO's radius of gyration differs from that of $\rho_{\text{spin}}(\mathbf{r})$ by only about 0.05 Å.[11]

The isotropic electron *g*-factor for e^-(aq) was measured long ago by EPR.[36,41,42,46−51] It deviates significantly from the free-electron value (g_{free} = 2.002319···), which is interpreted to mean that a fraction of the spin density must be supported in oxygen 2p orbitals.[40,41,50,51] That fraction has been estimated at 4% for alkaline aqueous glass at T = 77 K, based on the hyperfine spectra.[40] Measurements of the electronic absorption spectrum of e^-(aq) also indicate that water orbitals contribute to $\rho_{\text{spin}}(\mathbf{r})$, insofar as the integrated oscillator strength f = 1.14 exceeds unity, indicating intensity borrowing from solvent-centered electronic transitions.[52]

The contribution of the oxygen orbitals to $\rho_{\text{spin}}(\mathbf{r})$ is challenging to quantify precisely in a theoretical calculation because it is sensitive to definition and subject to substantial dynamical fluctuations that are documented herein. Nevertheless, numerous calculations are consistent with 10−20% of the spin density overlapping with the water molecules.[10,11,17,43,50,53] The rest resides within the cavity, and in the interstices between water molecules.

Most importantly for the present work, the *g*-factor for e^-(aq) has been measured at several different temperatures within the liquid range, from 9−45 °C (Table 1).[49,50] At higher temperatures, g moves further away from the free-electron value although the temperature-induced changes are small relative to the shift

$$\Delta g(T) = g(T) - g_{\text{free}} \quad (2)$$

at any given temperature. In the experimental paper reporting the $g(T)$ data,[49] the temperature dependence was considered puzzling insofar as it was interpreted to mean more participation by oxygen orbitals at higher temperature, where solvent fluctuations are enhanced.

In the present work, we quantify what this implies at a molecular level by means of *ab initio* MD simulations from T = 273 K (near and perhaps below the freezing transition, in our theoretical model) up to T = 373 K. Our results demonstrate that there is no inconsistency with the cavity picture of e^-(aq), which emerges naturally from the simulations (Figure 1). Rather than being inconsistent with a cavity picture, the increase in $|\Delta g(T)|$ with temperature reflects a cavity picture in which spin density on first-shell water molecules decreases very slightly as thermal fluctuations are amplified at higher temperature, shifting a small amount of spin density onto water molecules in the second solvation shell. We will demonstrate that both the cavity structure and the average coordination number are preserved across the entire temperature range of liquid water at 1 atm of pressure.

Table 1. Isotropic *g*-Factors for e^-(aq) from EPR

T (K)	g	Δg (ppm)[a]
282	2.00046 ± 0.00001[b]	−1859 ± 10
295	2.00047 ± 0.00007[c]	−1849 ± 70
296	2.00043 ± 0.00001[b]	−1889 ± 10
318	2.00038 ± 0.00001[b]	−1939 ± 10

[a]Equation 2; ppm = $(\Delta g) \times 10^6$. [b]Ref 49. [c]Ref 50.

2. METHODS

A poor choice of exchange-correlation functional will fail to localize e^-(aq),[54] due to well-known issues with self-interaction error when using semilocal functionals.[55,56] Our choice of functional is justified in Section 2.1, then the *ab initio* MD simulations are described in Section 2.2. Quantum chemistry calculations within a quantum mechanics/molecular mechanics (QM/MM) framework, as described in Section 2.3, are used to compute the *g*-factor and to quantify how much of the spin density is hosted by water molecules.

2.1. Exchange-Correlation Functional

Following previous simulations of water and aqueous radicals by Pasquarello and co-workers,[18,57−62] we used the PBEh(40)-rVV10 functional and the DZVP-GTH basis set, with PBEh(40)-GTH pseudopotentials parametrized for this particular functional.[63−65] Here, PBEh(40) means a hybrid of PBE exchange[66] with 40% "exact" (Hartree−Fock) exchange. The rVV10 functional is a revised version[67] of a nonlocal correlation functional for dispersion.[68]

The composite functional PBEh(40)-rVV10 affords a band gap of 8.75 eV for liquid water,[59] in good agreement with a widely quoted experimental estimate, E_{gap} = 8.7 ± 0.6 eV.[69] Some experimental estimates of the gap are significantly smaller than this ($E_{\text{gap}} \approx 7$ eV),[70,71] but not as small as the values afforded by semilocal functionals ($E_{\text{gap}} \sim 4$−5 eV).[72−75] A reasonable band gap for water is prerequisite for spectroscopic applications,[26] as excited states of the solute may otherwise appear as spurious midgap states of the solvent, and their wave functions can delocalize by accessing artificially low-energy conduction-band states.[72] Functionals with 40% Hartree−Fock exchange also afford reasonable estimates of the absorption band maximum of e^-(aq).[25,76]

Following recommendations from previous work on liquid water,[18] we set the short-range dispersion damping parameter[68] in rVV10 to b = 5.3. The original rVV10 value is b = 6.3,[67] and only minor differences in the structure of liquid water are observed over the range b = 5.3−9.3.[57−59] The choice b = 5.3 affords a liquid-state mass density of 1.02 g/cm^3 at T = 298 K,[59] in excellent agreement with experiment. Over the range b = 6.3−9.3, PBEh(40)-rVV10 simulations of liquid water afford an average of ≈3.6 hydrogen bonds per water molecule,[57] consistent with an experimental estimate under ambient conditions.[77] The choice b = 9.3 affords an equally good mass density as compared to smaller values of b,[57] but affords radial distribution functions (RDFs) that are overstructured with respect to experiment.[59]

2.2. Simulations

Ab initio MD simulations of e^-(aq) cannot be equilibrated in an aggressive way so we start from an equilibrated ground-state trajectory of I^-(aq),[26] then remove the iodine atom and leave an excess electron as part of the liquid's electronic structure. As in previous simulations of I^-(aq),[26] we use a cubic box (L = 14.3 Å) containing N = 96 water molecules, corresponding to the normal liquid density of 0.997 g/cm^3. Comparable simulations of e^-(aq) using the PBE0-D3 functional report no change in the position of the first and second solvation shells in the RDFs between simulation using N = 47, 64, and 128.[11] Thus, we expect the present simulations to adequately represent the liquid structure.

Simulations of the canonical ensemble (constant *NVT*) were propagated under periodic boundary conditions with a time step of

https://doi.org/10.1021/jacs.6c07020
J. Am. Chem. Soc. 2026, 148, 36675−36686

0.5 fs, using the CP2K program v. 2025.1.[78] Initially, we performed ∼20 ps of equilibration using velocity rescaling,[79] separately at temperatures T = 273, 298, 338, and 373 K. Production runs of 120 ps were then performed at each temperature using a Nosé-Hoover thermostat.[80] RDFs were generated using the TRAVIS program,[81] with a stride length of 5 fs and a bin width of 3.33 pm. These were subsequently smoothed using block averaging over three bins (0.1 Å).

Liquid water's density varies by only 4% across its entire temperature range at P = 1 atm.[82] Thus, to eliminate this confounding variable we employed the same density (0.997 g/cm^3) at each of the four temperatures indicated above. To validate this approach, another set of simulations was performed using water's experimental density at each temperature. RDFs for this second set of simulations exhibit the same solvation-shell structure as those performed using the ambient density; see Figure S1. Only the ambient-density simulations are used for the following analysis and discussion.

2.3. Quantum Chemistry Calculations

Structures were extracted from the simulations every 25 fs and properties were computed using a QM/MM scheme, averaging over 120 ps of production simulation at each temperature. Except where specified otherwise, the QM region in these calculations consists of all water molecules within 7 Å of the centroid of the maximally localized Wannier function[83] (MLWF) corresponding to the SOMO. These QM regions encompass 140−150 water molecules, significantly larger than what we have used in previous analyses of e^-(aq).[15,16,84,85] The remaining atoms from a 3 × 3 supercell were represented as MM point charges (q_H = +0.41 and q_O = −0.82).

Using this setup, the electron g-factor was computed at the PBEh(40)-VV10/6-31+G* level using the Orca program, v. 6.0.1.[86] This basis set has been tested for e^-(aq) in previous work and found to be reasonably well converged for condensed-phase calculations, e.g., for the optical spectrum.[15,85] On the other hand, this basis set would be inadequate for finite water cluster anions,[87] whose wave functions extend significantly into vacuum. However, the dense arrangement of water molecules in the liquid allows for converged or nearly converged simulations using only a single set of diffuse functions.[15,85] Data in Figure S2 demonstrate that the pcseg-2 basis set, which is triple-ζ quality and includes f-type polarization functions,[88] affords very similar values for Δg.

In order to quantify the spin density hosted by the water molecules, we also performed calculations at the PBEh(40)-rVV10/6-31+G* level using the aforementioned QM/MM setup, augmented by an additional floating center (ghost atom) placed at the centroid of the unpaired MLWF, determined instantaneously at each time step. The floating-center basis functions correspond to aug-cc-pVDZ for He. The DFT spin density was assigned to atoms using Becke's partition,[89] including Bragg-Slater atomic size corrections.[89−91] This is equivalent to the use of atomic Voronoi cells whose boundaries are smoothed by a switching function. As such, the ghost atom's Becke population corresponds to integration of $\rho_{spin}(\mathbf{r})$ over points $\mathbf{r}$ that are closer to the centroid of the SOMO than to any nucleus. Becke populations were computed using an Euler−Maclaurin−Lebedev grid with 99 radial points and 590 angular points,[92] whose quality has been appraised elsewhere.[87,93] This analysis was performed using Q-Chem v. 6.3.0,[94] as were calculations of the SOMO's radius of gyration (*vide infra*).

3. RESULTS AND DISCUSSION

The present simulations of $(H_2O)_{96}^-$ under periodic boundary conditions, with production runs of 120 ps at each of four temperatures, represent some of the largest and longest *ab initio* MD simulations of e^-(aq) performed to date. We will first characterize the liquid structure (Section 3.1), as quantified by RDFs for the $e^-\cdots$X distance (X = O or H). Subsequently, we examine the T-dependence of the g-factor (Section 3.2) and then quantify electron delocalization via atomic partition of the spin density (Section 3.3).

Each of these analyses is performed over temperatures ranging from 273−373 K. Normal melting and boiling temperatures for water described at the PBEh(40)-rVV10 level have not been reported, although temperature-dependent densities are in good agreement with experiment.[25] That said, classical water (omitting nuclear quantum effects) melts at 275 K when described using the hybrid revPBE0-D3 functional,[95,96] with a heat of vaporization that is only 7% lower than experiment.[96] Meanwhile, the hybrid PBE0-D3 functional affords an oxygen−oxygen RDF for liquid water that agrees with experiment to within the uncertainty of the latter.[97] Together, these observations suggest that the range of temperatures considered here should approximate the liquid range of the DFT water model that is employed. In any case, no phase transition is possible within our simulation setup.

3.1. Liquid Structure

RDFs for the $e^-\cdots$X distance (X = H or O), which we denote as $G_{eX}(r)$, are plotted in Figure 2 for each of the four

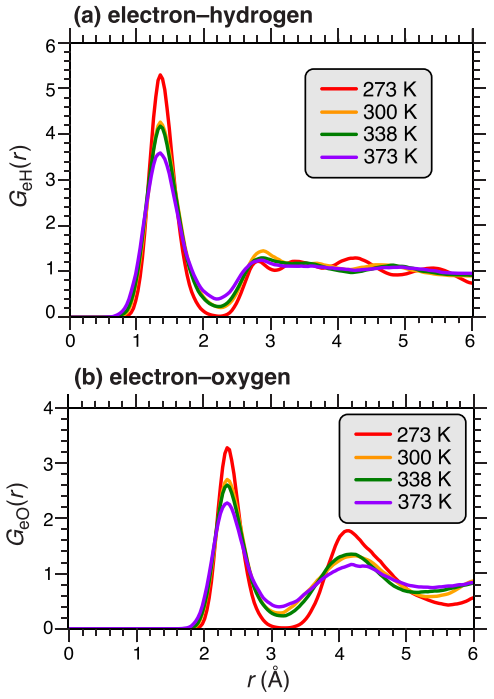

Figure 2. RDFs $G_{eX}(r)$ for (a) X = H and (b) X = O, obtained from 120 ps of production simulation data at each of the four temperatures indicated. The value r = 0 corresponds to the centroid of the unpaired MLWF.

temperatures simulated. The origin (r = 0) corresponds to the instantaneous centroid of the unpaired MLWF in the simulations. Evidence of a cavity can be found in the fact that $G_{eO}(r) \approx 0$ for $r \lesssim 2$ Å (Figure 2b). The size of the cavity is largely insensitive to temperature; the radius of the excluded volume changes by no more than 0.2 Å across the range of simulation temperatures. This is consistent with previous PBE0-D3 simulations at T = 298 and 350 K, although those simulations do indicate softening of the sharp turn-on in $G_{eO}(r)$ at T = 375 K.[11] This is not observed in the present simulations, which are much longer (120 ps versus ∼20 ps) and also larger (N = 96 versus N = 64) as compared to the simulations reported in ref 11. However, the present

https://doi.org/10.1021/jacs.6c07020
J. Am. Chem. Soc. 2026, 148, 36675−36686

Table 2. Ensemble-Averaged Properties of e^-(aq) from *ab Initio* MD Simulations[a]

T (K)	$\langle r_{HB}\rangle$[b] (Å)	$\langle r_{gyr}\rangle$[c] (Å)	$\langle n_{HB}\rangle$[d]	$\langle n_2\rangle$[e]	$\langle \Delta g\rangle$ (ppm)[f]
273	1.350 ± 0.414	2.413 ± 0.236	3.997 ± 0.082	24.645 ± 1.032	−1488 ± 146
300	1.383 ± 0.512	2.398 ± 0.211	4.318 ± 0.560	22.915 ± 1.453	−1560 ± 150
338	1.350 ± 0.518	2.487 ± 0.257	4.203 ± 0.484	18.793 ± 1.703	−1600 ± 161
373	1.317 ± 0.562	2.487 ± 0.249	4.216 ± 0.577	18.637 ± 1.717	−1660 ± 174

[a]Error bars indicate one standard deviation, using 120 ps of simulation data at each temperature. See Table S2 for block-averaged values and estimates of the standard errors in the mean values. [b]From a Gaussian fit of the first peak in $G_{eH}(r)$. [c]Equation 3, computed for the SOMO using QM/MM snapshots. [d]Number of hydrogen atoms in the first solvation shell of e^-(aq); see Figure S3. [e]Number of oxygen atoms in the first two solvation shells of e^-(aq); see Figure S4. [f]Computed from QM/MM snapshots.

simulations use a double-ζ basis set rather than the triple-ζ basis that is used in ref 11.

The size of the first solvation shell is remarkably consistent with results from cavity-forming one-electron pseudopotential models.[7] However, the liquid is much more structured in the DFT simulations,[11] and that structure is remarkably insensitive to temperature. In contemplating that result, it is worth considering that the well depth of the electron−water interaction ∼50 kcal/mol,[7] an order of magnitude stronger than a water−water hydrogen bond.[98,99] It is also significantly larger than halide−water interaction energies,[90] or those of other monovalent ions with water.[100] Meanwhile, k_BT = 0.5 kcal/mol at T = 273 K and is only 0.8 kcal/mol at 373 K. While solvent fluctuations should increase at higher temperature, on purely energetic grounds it is not altogether surprising that the average solvation structure of e^-(aq) is qualitatively insensitive to temperature across the liquid range.

From $G_{eH}(r)$ in Figure 2a, one may infer an electron−water hydrogen-bond distance $\langle r_{HB}\rangle$ = 1.3−1.4 Å. Numerical averages for this and other properties are provided in Table 2, with standard deviations that quantify fluctuations in their instantaneous values. (See Table S2 for standard errors in the mean values.) The range of $\langle r_{HB}\rangle$ values is comparable to the hydrogen-bond distance $r_{F\cdots H}$ = 1.37 Å in the gas-phase $F^-(H_2O)$ complex but much shorter than the corresponding distance $r_{Cl\cdots H}$ = 2.1 Å in $Cl^-(H_2O)$.[90] The latter value is elongated to $\langle r_{Cl\cdots H}\rangle$ = 2.3−2.5 Å in Cl^-(aq).[101,102]

Although the average ion−water distance $\langle r_{HB}\rangle$ is largely insensitive to temperature, the distribution of instantaneous r_{HB} values does broaden at higher temperature. This is evident from both the reduced height of the first peak in $G_{eH}(r)$ (Figure 2a), and in the standard deviations for $\langle r_{HB}\rangle$ that are provided in Table 2. The position of the second solvation shell is somewhat more sensitive to temperature as compared to the first, consistent with results from other *ab initio* MD simulations.[11] For T = 273 K, both $G_{eH}(r)$ and $G_{eO}(r)$ go very nearly to zero between the first and second solvation shells, indicating a highly structured solvent that may represent a supercooled liquid. Even so, simulations at this temperature are worth considering because they provide one end point along a continuum of T-dependent dynamics within the liquid phase. Autocorrelation functions $\langle \mathbf{v}(t)\cdot\mathbf{v}(0)\rangle$ for the instantaneous H_2O bisector angles $\mathbf{v}(t)$ reveal significant librational dynamics even at T = 273 K; see Figure S5.

Average coordination numbers $\langle n_{HB}\rangle$ are provided in Table 2. These are obtained by integrating the coordination number $n_H(r)$ up to the first local minimum in $G_{eH}(r)$, as illustrated in Figure 3 for T = 273 K and 373 K. (For other temperatures, see Figure S3). The value $\langle n_{HB}\rangle$ = 4.3 that we obtain at T = 300 K is only slightly smaller than the value of 4.7 that is reported in similar simulations.[18] Table 2 also reports $\langle n_2\rangle$, the

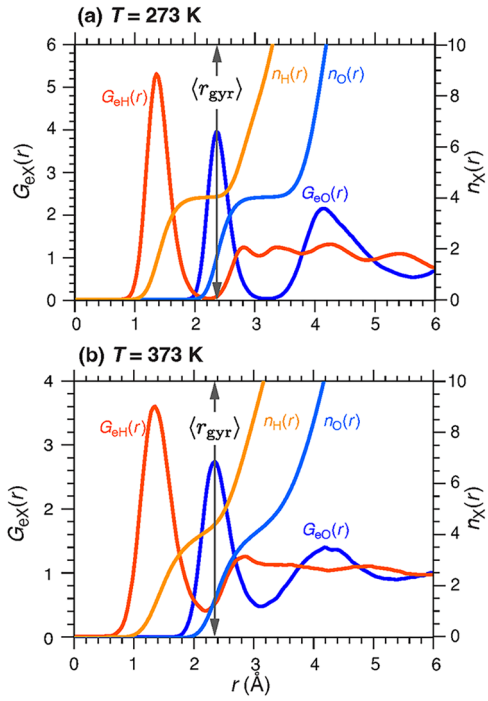

Figure 3. RDFs $G_{eX}(r)$ at (a) T = 273 K and (b) T = 373 K, to be read from the scale on the left, and integrated coordination numbers $n_X(r)$, to be read from the scale on the right. The value of $\langle r_{gyr}\rangle$ is indicated using gray arrows.

average number of oxygen atoms in the first two solvation shells, computed as shown in Figure S4. The value $\langle n_2\rangle$ is a proxy for the number of water molecules in the first two solvation shells.

In examining the RDFs for e^-(aq), the size of the electron's wave function should be considered. This can be quantified in terms of its radius of gyration

$$r_{gyr} = \left(\langle r^2\rangle - \langle \mathbf{r}\rangle\cdot\langle \mathbf{r}\rangle\right)^{1/2} \quad (3)$$

As explained and quantified elsewhere,[26] the instantaneous size of the unpaired MLWF in *ab initio* MD simulations of e^-(aq) is significantly smaller than the radius of gyration of $\rho_{spin}(\mathbf{r})$. As such, we compute r_{gyr} in eq 3 from QM/MM snapshots using the ghost atom setup described in Section 2.3, taking the SOMO from those calculations as a proxy for $\rho_{spin}(\mathbf{r})$.

Ensemble-averaged values of $\langle r_{gyr}\rangle$ at each temperature can be found in Table 2. The value $\langle r_{gyr}\rangle$ = 2.40 ± 0.21 Å that we obtain at T = 300 K is similar to the value reported elsewhere (2.49 ± 0.12 Å) for simulations under ambient conditions using the same functional,[18] although somewhat larger than what is reported for PBE0-D3 simulations in a box with N =

https://doi.org/10.1021/jacs.6c07020
J. Am. Chem. Soc. 2026, 148, 36675−36686

128 water molecules (2.31 ± 0.08 Å).[11] Another recent PBE0-D3 simulation with N = 64 reports $\langle r_{gyr}\rangle$ = 2.1 Å,[56] indicating some sensitivity with regard to simulation setup. In any case, our PBEh(40)-rVV10 result is close to experimental estimates of 2.42−2.45 Å at T = 298 K.[6,103−106] These are inferred from the band shape of the absorption spectrum, which can be related to $\langle r_{gyr}\rangle$ within a one-electron treatment.[52,103,106−110]

The ensemble-averaged radius of gyration is only weakly dependent on temperature in our simulations, increasing to $\langle r_{gyr}\rangle$ = 2.49 ± 0.25 Å at T = 373 K. In contrast, a value of 2.64 Å is estimated from the experimental absorption spectrum at T = 363 K.[103] Values $\langle r_{gyr}\rangle$ = 2.54 ± 0.19 Å (at 350 K) and $\langle r_{gyr}\rangle$ = 2.62 ± 0.24 Å (at 375 K) are obtained from periodic PBE0-D3 simulations using short simulations with N = 64 water molecules.[11] These comparisons may suggest that the extent of fluctuations at higher temperatures is underestimated by the present simulations. Near the freezing temperature, the experimental estimate is $\langle r_{gyr}\rangle$ = 2.42 Å (at 274 K),[108] whereas our value at the opposite end of the liquid range is 2.49 ± 0.25 Å (at 373 K).

Other *ab initio* MD simulations also reveal relatively small shifts in $\langle r_{gyr}\rangle$ as a function of temperature. For example, in *NPT* simulations at P = 250 bar, the radius of gyration shifts from $\langle r_{gyr}\rangle$ = 2.31 Å at T = 423 K, to 2.41 Å at T = 473 K, and finally to $\langle r_{gyr}\rangle$ = 2.49 Å at T = 523 K.[25] While these relatively subtle shifts are responsible for T-dependent shifts that have been carefully measured in the absorption maximum of e^-(aq),[104−106] they have no qualitative bearing on the picture of an electron in an excluded volume. Furthermore, the electronic absorption spectrum of e^-(aq) is not diagnostic of its structure.[6] In the present work, that spectrum was computed at each temperature using linear-response DFT,[111] in conjunction with an optimally tuned,[112,113] long-range corrected functional.[114] Temperature-dependent shifts in the computed spectrum (Figure S6) are consistent with similar calculations reported elsewhere.[11]

Upon placing $\langle r_{gyr}\rangle$ onto the RDFs, as in Figure 3, it is clear that the tail of the electron's wave function completely envelopes the coordinating hydrogen atoms of the first-shell water molecules. In fact, $\langle r_{gyr}\rangle$ extends over most of the first-shell peak in $G_{eO}(r)$ as well, consistent with inferences from various spectroscopies as discussed in Section 1. That the coordination motif is monodentate rather than bidentate is evident from the snapshot in Figure 1 and has been deduced from isotopic shifts in resonance Raman spectra.[6,20,115]

Juxtaposing RDFs at the highest and lowest temperatures simulated (Figure 3), which bookend the liquid-phase temperature range, emphasizes how little the structure of e^-(aq) changes as a function of temperature. Recent simulations of the hydration entropy ($\Delta S^{\ominus}_{hyd}$) of e^-(aq) suggest that DFT may overestimate the structure of this species,[116] consistent with the idea that dynamical fluctuations may be somewhat suppressed in the present simulations. Nevertheless, the absence of any qualitative change in the structure of e^-(aq) as a function of temperature is striking.

3.2. Electron *g*-Factor

The isotropic g-factor of e^-(aq) was obtained by extracting snapshots from the simulations and considering these as finite QM/MM calculations, as described in Section 2.3. Results are plotted in Figure 4 for each simulation temperature, demonstrating both the breadth of the fluctuations and convergence of the averaging. Reminiscent of simulations

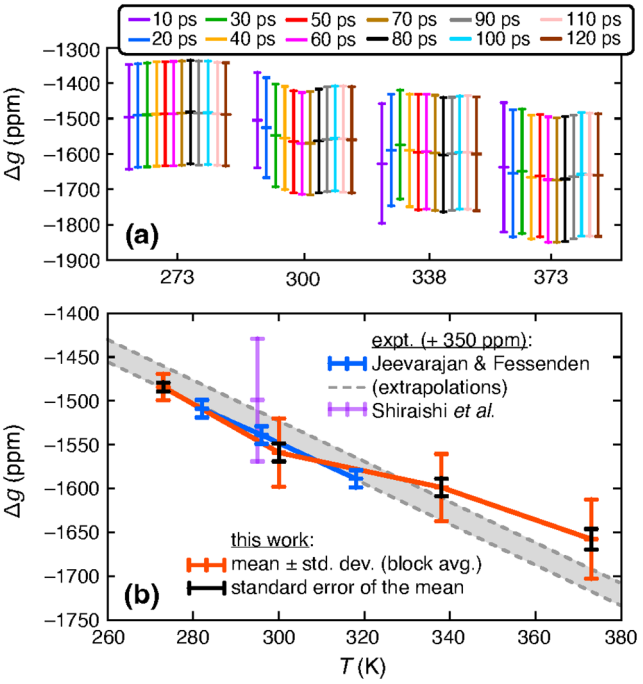

Figure 4. Distribution of Δg values at each simulation temperature. (a) Cumulative averages from 10−120 ps of simulation data, with whiskers to indicate one standard deviation above and below the mean value, $\langle\Delta g\rangle$. (b) Block-averaged results in comparison to experimental data from Table 1 that have been shifted by 350 ppm. Whiskers extend to one standard deviation above and below the mean and standard errors in the block-averaged mean values are also shown. Experimental data from ref 49. have been extrapolated across the whole temperature range using either a 350 ppm shift (lower dashed line) or a 375 ppm shift (upper dashed line).

that reproduce the T-dependent shift in the absorption maximum,[25] changes in $\langle\Delta g\rangle(T)$ are small compared to the magnitude of the fluctuations at any given temperature (Figure 4a). Obtaining a monotonic shift requires 40−50 ps of averaging, but ultimately the monotonic shift that is observed experimentally over the range T = 282−318 K[49] is reproduced across the whole liquid temperature range in our simulations. Reverse-time averages analogous to Figure 4a are plotted in Figure S9 and show similar behavior, with 40−50 ps required to obtain convergence.

Figure 4b plots T-dependent values of $\langle\Delta g\rangle$, comparing theory and experiment. The experimental values have been shifted by 350 ppm from the measurements in Table 1 in order to put them on the scale of the simulations. This shift represents the current limitations of DFT for g-factor calculations, as even state-of-the-art double-hybrid functionals exhibit mean unsigned errors of ∼400 ppm.[117] Nevertheless, a broad survey of radicals suggests that the shifts are systematic and that DFT calculations correlate extremely well with experiment (R^2 = 0.988), despite a systematic shift that scales with the magnitude of $\langle\Delta g\rangle$.[117] This suggests that T-dependent trends reported here are meaningful, despite the 350 ppm shift that is required to match experiment.

This satisfactory agreement is interesting in view of the fact that our simulations suggest no qualitative change in the structure of e^-(aq) from 0−100 °C at atmospheric pressure. In the experimental report of the $\langle\Delta g\rangle(T)$ data,[49] the investigators questioned how a further shift away from g_{free} at elevated temperature—even if small—could be rationalized in

https://doi.org/10.1021/jacs.6c07020
J. Am. Chem. Soc. 2026, 148, 36675−36686

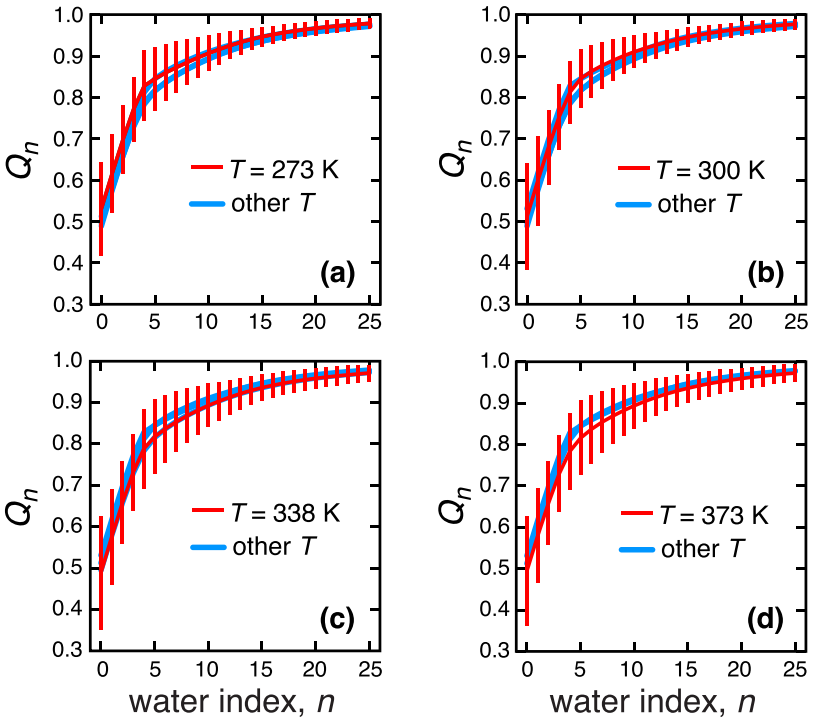

Figure 5. Cumulative spin charge Q_n (eq 4) from Becke population analysis, starting with the ghost atom (n = 0) then accumulating each q_{Wn} in order of increasing distance from the centroid of the SOMO. Results are shown for snapshots taken from simulations at (a) T = 273 K, (b) T = 300 K, (c) T = 338 K, and (d) T = 373 K. The red curve in each panel connects mean values $\langle Q_n \rangle$ at each n, averaged over 120 ps, with whiskers representing one standard deviation above and below the mean. Mean values at other temperatures are shown in blue (without standard deviations), to emphasize subtle changes as a function of temperature. Calculations were performed using a QM/MM scheme at the PBEh(40)-rVV10/6-31+G* level.

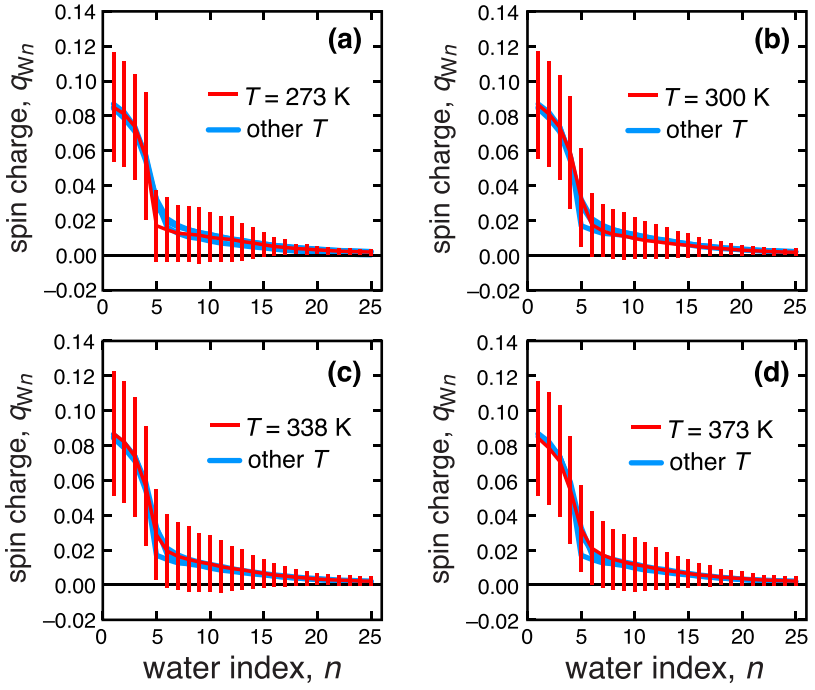

Figure 6. Spin charge q_{Wn} on each water molecule, computed using Becke partition and arranged in order of increasing distance from the ghost atom at the centroid of the SOMO, for (a) T = 273 K, (b) T = 300 K, (c) T = 338 K, and (d) T = 373 K. The red curve in each panel connects mean values $\langle q_{Wn} \rangle$ at each n, with whiskers representing one standard deviation above and below the mean. Mean values at other temperatures are shown in blue (without standard deviations), to emphasize the inflection point near n = 5. Calculations were performed using a QM/MM scheme at the PBEh(40)-rVV10/6-31+G* level.

terms of a cavity-localized electron. They note two key facts: first, that the solvation shell should be less tightly bound at higher temperature; and second, that the magnitude of $\langle \Delta g \rangle(T)$ nevertheless suggests increased participation by

https://doi.org/10.1021/jacs.6c07020
J. Am. Chem. Soc. 2026, 148, 36675−36686

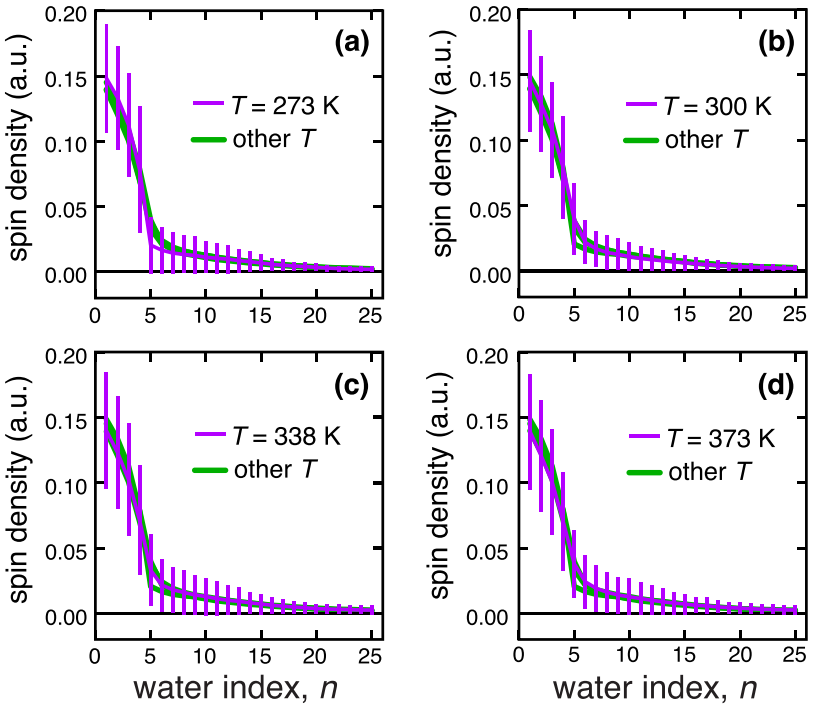

Figure 7. Spin densities at the oxygen nuclei, sorted according to their distance from a ghost atom that is located at the centroid of the SOMO, for e^-(aq) simulations at (a) T = 273 K, (b) T = 300 K, (c) T = 338 K, and (d) T = 373 K. Purple curves in each panel connect the ensemble-averaged mean value at each nucleus, with whiskers representing one standard deviation above and below the mean. Mean values at other temperatures are shown in green (without standard deviations), to emphasize subtle changes as a function of temperature. Calculations were performed at the PBEh(40)-rVV10/6-31+G* level using a QM/MM scheme, averaging over a Gaussian function at the nucleus whose width is 0.25 bohr.

oxygen orbitals at higher temperature. The second part of this reasoning is investigated in Section 3.3 using population analysis, but the first observation can be addressed immediately.

A "looser" solvation structure at higher temperature means *slightly* broader features in the RDFs, which implies broader distributions in r_{HB} as quantified by standard deviations in Table 2. The electron's first solvation shell is defined by the first local minimum in either $G_{eH}(r)$ or $G_{eO}(r)$, and the values of both RDFs at those local minima increase as a function of temperature (Figure 2). This suggests that the distinction between the two solvation shells is less pronounced—although certainly not lost—at elevated temperature. This is especially clear from plots of the integrated coordination numbers $n_X(r)$ at T = 373 K (Figure 3b). Overall, however, these temperature-dependent changes are rather small. A well-defined cavity structure is evidently preserved even at T = 373 K.

3.3. Spin Density Delocalization

We next examine how the spin density is partitioned onto atoms. Population analysis applied to $\rho_{spin}(\mathbf{r})$ affords *spin charges* for each atom,[118,119] which sum to +1 for a single unpaired electron. To obtain a spin charge for the cavity, we place a ghost atom at the centroid of the SOMO,[120] determined separately at each snapshot. Spin charges are computed using Becke partition[89] and the ensemble-averaged spin charge associated with the ghost atom is $\langle q_{Gh}\rangle$ = 0.48−0.53, depending on temperature. This leaves about half of the spin density to be distributed across the water molecules.

The spin charge on any given atom fluctuates rapidly, with a correlation time of ∼10 fs for the spin density on a given oxygen nucleus (see Figure S9). To obtain static probability distributions, we sum the atomic populations on each water molecule to obtain its total spin charge. These are denoted q_{W1}, q_{W2}, ..., where q_{Wn} is the spin charge on the nth closest water molecule to the center of the SOMO. Distances are recomputed for each snapshot, so $q_{W1}(t)$ represents the spin charge on whichever molecule is nearest to the ghost atom at time t.

Figure 5 plots the cumulative value of the spin charge, starting with the ghost atom and accumulating in order of each water molecule's distance from the centroid of the SOMO. This cumulative charge is defined as

$$Q_n = q_{Gh} + \sum_{k=1}^{n} q_{Wk} \tag{4}$$

with $Q_0 = q_{Gh}$, the ghost-atom spin charge. At T = 273 K, the 25 water molecules that are included in Figure 5 constitute two solvation shells around the electron, according to $\langle n_2\rangle$ in Table 2. At higher temperatures there are slightly fewer water molecules in the first two solvation shells, with $\langle n_2\rangle$ = 19−23. Plots in Figure 5 demonstrate convergence within two solvation shells ($Q_{25} \approx 1$), consistent with other theoretical analyses that reached the same conclusion.[7−9]

Figure 6 plots individual values q_{W1}, q_{W2}, ..., which decay to zero as n increases. Evident across the entire temperature range is a clear break in the magnitude of q_{Wn} between n = 4 and n = 5. (Mulliken spin charges afford similar behavior as shown in Figures S10 and S11). We interpret this as a sharp change in the spin charge beyond the first solvation shell, consistent with the fact that $\langle n_{HB}\rangle$ ranges from 4.0−4.3 across the simulated temperature range (Table 2). These values of $\langle n_{HB}\rangle$ are slightly smaller than the average coordination number of 4.7 that is reported elsewhere,[18] for simulations at T = 298 K using the same exchange-correlation functional. In that work, however,

https://doi.org/10.1021/jacs.6c07020
J. Am. Chem. Soc. 2026, 148, 36675−36686

$\langle r_{gyr} \rangle$ was used as a cutoff for integrating $n_H(r)$, whereas we use the first minimum in $G_{eH}(r)$ to define $\langle n_{HB} \rangle$. As evident from Figure 3, ours is a slightly smaller cutoff leading to a slightly smaller coordination number.

Values of q_{Wn} drop sharply beyond the first solvation shell (i.e., for $n > 4$), especially at 273 K and to a slightly lesser extent at higher temperatures. In all cases, the mean value $\langle q_{Wn} \rangle$ decays monotonically with n, meaning monotonically with distance from the ghost atom. By the time one reaches the water molecule with $n = \langle n_2 \rangle$, indicating the far edge of the second solvation shell, the spin charge q_{Wn} has decayed essentially to zero. This conclusion holds even at higher temperatures where $\langle n_2 \rangle$ is smaller, as a result of thermal broadening of the second-shell peak in $G_{eO}(r)$. Even at $T = 373$ K, there is no evidence of electron penetration into the third solvation shell.

As an alternative measure of e^-(aq) penetration into solvent molecules, we compute the spin density at the oxygen nuclei. Lack of nuclear cusps in Gaussian basis sets presents challenges for doing so, but these artifacts can be mitigated by averaging over a narrow Gaussian function centered on the nucleus, rather than a δ-function.[121−123] Spin densities at the oxygen nuclei, computed in this way and sorted according to the distance from the centroid of the SOMO, are shown in Figure 7. These quantities decay in a manner that is remarkably similar to the Becke charges q_{Wn} in Figure 6. This analysis further supports the idea that the spin density is entirely contained within two solvation shells.

What is also remarkable is how little the distribution of spin densities changes as a function of temperature, despite a clear T-dependent shift in the g-factor that is recovered from our calculations. An explanation can be found by overlaying the Q_n and q_{Wn} plots at different temperatures, as we have done in Figures 5 and 6. What is observed in either case is that the fraction of ρ_{spin} that is hosted on the first-shell water molecules (indices 1−5 in Figures 5 and 6) is largest at $T = 273$ K and smallest at $T = 373$ K. The total spin charge integrates to unity, so this change must be offset by a reciprocal temperature dependence for the spin charge on the remaining water molecules. The result is an inflection point at q_{W5} in Figure 6, such that the values q_{W6}, q_{W7}, ... are largest at the highest temperature. This is the manner in which higher temperature manifests as additional spin density hosted on water molecules beyond the first solvation shell.

4. CONCLUSIONS

The absorption spectrum of e^-(aq) has been measured across a wide range of temperatures.[106] Its maximum shifts to lower energy by a small but continuous amount (≈2.4−2.8 meV/K) as the temperature increases,[104,105] which has previously been rationalized within the cavity model of the aqueous electron.[25,124,125] The electronic absorption spectrum of e^-(aq) has also been measured in both supercooled water[105] and in supercritical water.[104] The T-dependent shift in the absorption maximum continues uninterrupted into these superlative regimes, without any abrupt transition. The absence of a distinct transition provides indirect evidence that there might also be no abrupt structural change.

That notion is bolstered by the simulations presented here, which exhibit no discontinuous changes in cavity structure across the whole liquid temperature range from $T = 273$ K (possibly supercooled, in our simulations) up to $T = 373$ K. This behavior for e^-(aq) is consistent with the fact that hydration of classical monovalent ions continues to be bulk-like even in supercritical water at low average densities,[126−128] due to density inhomogeneities that favor clustering and accommodate solutes in regions of bulk-like density.[129,130]

Experiments also reveal that the molar extinction coefficient for e^-(aq), evaluated at the absorption maximum, is essentially independent of temperature from $T = 295$−623 K.[52] This is consistent with the present analysis, indicating that charge penetration onto the solvent molecules is only weakly dependent on temperature with changes that are hardly discernible except near the freezing temperature.

The present simulations recover the T-dependent shift in the EPR g-factor for e^-(aq) and suggest that it is a collective effect of increasing fluctuations at higher temperatures, especially the softening of the second solvation shell of oxygen atoms and increasing fluctuations in the ion−water hydrogen bonds. Our simulations are consistent with a cavity model of e^-(aq), even at 100 °C, and this is consistent with known spectroscopic data for this exotic species. Together with a long list of other physical observables that are better explained by a localized rather than a delocalized structure for e^-(aq),[6] and recent experiments strongly favoring a localized structure,[32] the overwhelming weight of evidence favors a particle-in-a-solvent-void model for e^-(aq).

■ ASSOCIATED CONTENT

Supporting Information

The Supporting Information is available free of charge at https://pubs.acs.org/doi/10.1021/jacs.6c07020.

Additional RDFs, correlation functions, statistical analyses, and Mulliken populations (PDF)

■ AUTHOR INFORMATION

Corresponding Author

John M. Herbert − *Dept. of Chemistry & Biochemistry, The Ohio State University, Columbus, Ohio 43210, United States;* orcid.org/0000-0002-1663-2278; Email: herbert@chemistry.ohio-state.edu

Authors

Ar. M. Fonlon − *Dept. of Chemistry & Biochemistry, The Ohio State University, Columbus, Ohio 43210, United States*

Christopher J. Mundy − *Physical Science Division, Pacific Northwest National Laboratory, Richland, Washington 99352, United States;* orcid.org/0000-0003-1378-5241

Complete contact information is available at: https://pubs.acs.org/10.1021/jacs.6c07020

Notes

The authors declare the following competing financial interest(s): J.M.H. is part owner of Q-Chem Inc. and serves on its board of directors.

■ ACKNOWLEDGMENTS

This work is dedicated to the memory of Pavel Jungwirth (deceased 23 July, 2026), an energetic scientist and—more importantly—a compassionate human being. Work by A.M.F. and J.M.H. was supported by the National Science Foundation, grant no. CHE-2402361. A.M.F. also acknowledges funding from the Ohio State Chemistry Bridge Program. Work by C.J.M. was supported by the U.S. Department of Energy

(DOE), Office of Science, Basic Energy Sciences (BES), Chemical Sciences, Geosciences, and Biosciences Division, Chemical Physics and Interfacial Sciences Program, FWP 16249. Calculations were performed at the Ohio Supercomputer Center.[131]

REFERENCES

(1) Mozumder, A. The Solvated Electron. In *Fundamentals of Radiation Chemistry*; Academic Press: San Diego, CA, 1999, Chapter 6; pp 145−198.
(2) Mostafavi, M.; Lampre, I. The Solvated Electron: A Singular Chemical Species. In *Radiation Chemistry: From Basics to Applications in Material and Life Sciences*; Spotheim-Maurizot, M.; Mostafavi, M.; Belloni, J.; Douki, T., Eds.; EDP Sciences, 2008, Chapter 3; pp 33−52.
(3) Buxton, G. V. An Overview of the Radiation Chemistry of Liquids. In *Radiation Chemistry: From Basics to Applications in Material and Life Sciences*; Spotheim-Maurizot, M.; Mostafavi, M.; Belloni, J.; Douki, T., Eds.; EDP Sciences, 2008, Chapter 1; pp 3−16.
(4) Alizadeh, E.; Sanche, L. Precursors of solvated electrons in radiobiological physics and chemistry. *Chem. Rev.* **2012**, *112*, 5578−5602.
(5) Herbert, J. M.; Coons, M. P. The hydrated electron. *Annu. Rev. Phys. Chem.* **2017**, *68*, 447−472.
(6) Herbert, J. M. Structure of the aqueous electron. *Phys. Chem. Chem. Phys.* **2019**, *21*, 20538−20565.
(7) Jacobson, L. D.; Herbert, J. M. A one-electron model for the aqueous electron that includes many-body electron-water polarization: Bulk equilibrium structure, vertical electron binding energy, and optical absorption spectrum. *J. Chem. Phys.* **2010**, *133*, No. 154506.
(8) Williams, C. F.; Herbert, J. M. Influence of structure on electron correlation effects and electron−water dispersion interactions in anionic water clusters. *J. Phys. Chem. A* **2008**, *112*, 6171−6178.
(9) Herbert, J. M.; Jacobson, L. D. Nature's most squishy ion: The important role of solvent polarization in the description of the hydrated electron. *Int. Rev. Phys. Chem.* **2011**, *30*, 1−48.
(10) Uhlig, F.; Marsalek, O.; Jungwirth, P. Unraveling the complex nature of the hydrated electron. *J. Phys. Chem. Lett.* **2012**, *3*, 3071−3075.
(11) Park, S. J.; Schwartz, B. J. Understanding the temperature dependence and finite size effects in ab initio MD simulations of the hydrated electron. *J. Chem. Theory Comput.* **2022**, *18*, 4973−4982.
(12) Turi, L.; Rossky, P. J. Theoretical studies of spectroscopy and dynamics of hydrated electrons. *Chem. Rev.* **2012**, *112*, 5641−5674.
(13) Marsalek, O.; Uhlig, F.; VandeVondele, J.; Jungwirth, P. Structure, dynamics, and reactivity of hydrated electrons by ab initio molecular dynamics. *Acc. Chem. Res.* **2012**, *45*, 23−32.
(14) Uhlig, F.; Marsalek, O.; Jungwirth, P. Electron at the surface of water: Dehydrated or not? *J. Phys. Chem. Lett.* **2013**, *4*, 338−343.
(15) Uhlig, F.; Herbert, J. M.; Coons, M. P.; Jungwirth, P. Optical spectroscopy of the bulk and interfacial hydrated electron from ab initio calculations. *J. Phys. Chem. A* **2014**, *118*, 7507−7515.
(16) Coons, M. P.; You, Z.-Q.; Herbert, J. M. The hydrated electron at the surface of neat liquid water appears to be indistinguishable from the bulk species. *J. Am. Chem. Soc.* **2016**, *138*, 10879−10886.
(17) Kumar, A.; Walker, J. A.; Bartels, D. M.; Sevilla, M. D. A simple ab initio model for the hydrated electron that matches experiment. *J. Phys. Chem. A* **2015**, *119*, 9148−9159.
(18) Ambrosio, F.; Miceli, G.; Pasquarello, A. Electronic levels of excess electrons in liquid water. *J. Phys. Chem. Lett.* **2017**, *8*, 2055−2059.
(19) Pizzochero, M.; Ambrosio, F.; Pasquarello, A. Picture of the wet electron: A localized transient state in liquid water. *Chem. Sci.* **2019**, *10*, 7442−7448.
(20) Dasgupta, S.; Rana, B.; Herbert, J. M. *Ab initio* investigation of the resonance Raman spectrum of the hydrated electron. *J. Phys. Chem. B* **2019**, *123*, 8074−8084.
(21) Holden, Z. C.; Rana, B.; Herbert, J. M. Analytic energy gradients for the QM/MM-Ewald method using atomic charges derived from the electrostatic potential: Theory, implementation, and application to *ab initio* molecular dynamics of the aqueous electron. *J. Chem. Phys.* **2019**, *150*, No. 144115.
(22) Shen, Z.; Peng, S.; Glover, W. J. Flexible boundary layer using exchange for embedding theories. II. QM/MM dynamics of the hydrated electron. *J. Chem. Phys.* **2021**, *155*, No. 224113.
(23) Li, X.; Jia, X.; Paz, A. S. P.; Cao, Y.; Glover, W. J. Evidence for water antibonding orbital mixing in the hydrated electron from its oxygen 1s x-ray absorption spectrum. *J. Am. Chem. Soc.* **2022**, *144*, 19668−19672.
(24) Wilhelm, J.; VandeVondele, J.; Rybkin, V. V. Dynamics of the bulk hydrated electron from many-body wave-function theory. *Angew. Chem., Int. Ed.* **2019**, *58*, 3890−3893.
(25) Lan, J.; Rybkin, V. V.; Pasquarello, A. Temperature dependent properties of the aqueous electron. *Angew. Chem., Int. Ed.* **2022**, *61*, No. e202209398.
(26) Carter-Fenk, K.; Johnson, B. A.; Herbert, J. M.; Schenter, G. K.; Mundy, C. J. Birth of the hydrated electron via charge-transfer-to-solvent excitation of aqueous iodide. *J. Phys. Chem. Lett.* **2023**, *14*, 870−878.
(27) Mirón, G. D.; Malosso, C.; Di Pino, S.; Egan, C. K.; Dasgupta, D.; Mundy, C. J.; Hassanali, A. Simulating the photochemical birth of the hydrated electron in liquid water. *Nat. Commun.* **2026**, *17*, No. 3764.
(28) Janik, I.; Lisovskaya, A.; Bartels, D. M. Partial molar volume of the hydrated electron. *J. Phys. Chem. Lett.* **2019**, *10*, 2220−2226.
(29) Savolainen, J.; Uhlig, F.; Ahmed, S.; Hamm, P.; Jungwirth, P. Direct observation of the collapse of the delocalized excess electron in water. *Nat. Chem.* **2014**, *6*, 697−701.
(30) Low, P. J.; Chu, W.; Nie, Z.; Bin Mohd Yusof, M. S.; Prezhdo, O. V.; Loh, Z.-H. Observation of a transient intermediate in the ultrafast relaxation dynamics of the excess electron in strong-field-ionized liquid water. *Nat. Commun.* **2022**, *13*, No. 7300.
(31) Novelli, F.; Chen, K.; Buchmann, A.; Ockelmann, T.; Hoberg, C.; Head-Gordon, T.; Havenith, M. The birth and evolution of solvated electrons in the water. *Proc. Natl. Acad. Sci. U.S.A.* **2023**, *120*, No. e2216480120.
(32) Sopena Moros, A.; Li, S.; Li, K.; et al. Tracking cavity formation in electron solvation: Insights from x-ray spectroscopy and theory. *J. Am. Chem. Soc.* **2024**, *146*, 3262−3269.
(33) Jordan, C. J. C.; Coons, M. P.; Herbert, J. M.; Verlet, J. R. R. Spectroscopy and dynamics of the hydrated electron at the water/air interface. *Nat. Commun.* **2024**, *15*, No. 182.
(34) Matsuzaki, K.; Kuramochi, H.; Tahara, T. Electron confinement within a fluctuation "box" in liquid water, arXiv:2603.12537. arXiv.org e-Print archive, 2026 https://arxiv.org/abs/2603.12537.
(35) Bennett, J. E.; Mile, B.; Thomas, A. Electron spin resonance spectra of hydrated electrons prepared by reaction of atomic sodium with ice at 77° K. *Nature* **1964**, *201*, 919−920.
(36) Bennett, J. E.; Mile, B.; Thomas, A. Trapped electrons produced by the deposition of alkali-metal atoms on ice and solid alcohols at 77°K. Part I. Optical spectra and electron spin resonance spectra. *J. Chem. Soc. A* **1967**, *0*, 1393−1399.
(37) Narayana, P. A.; Bowman, M. K.; Kevan, L.; Yudanov, V. F.; Tsvetkov, Y. D. Electron spin echo envelope modulation of trapped radicals in disordered glassy systems: Application to the molecular structure around excess electrons in γ-irradiated 10 *M* sodium hydroxide alkaline ice glass. *J. Chem. Phys.* **1975**, *63*, 3365−3371.
(38) Kevan, L. Electron spin echo studies of solvation structure. *J. Phys. Chem. A* **1981**, *85*, 1628−1636.
(39) Kevan, L. Geometrical structure of solvated electrons. *Radiat. Phys. Chem.* **1981**, *17*, 413−423.
(40) Kevan, L. Solvated electron structure in glassy matrices. *Acc. Chem. Res.* **1981**, *14*, 138−145.
(41) Schlick, S.; Narayana, P. A.; Kevan, L. ESR line shape studies of trapped electrons in γ-irradiated ^{17}O enriched 10*M* NaOH alkaline ice

https://doi.org/10.1021/jacs.6c07020
J. Am. Chem. Soc. 2026, 148, 36675−36686

glass: Model for the geometrical structure of the trapped electron. *J. Chem. Phys.* **1976**, *64*, 3153−3160.
(42) Lin, D. P.; Kevan, L. Second moment studies of the electron spin resonance line shape of trapped electrons in sodium-ice condensates. Relation to the molecular structure around trapped electrons. *J. Phys. Chem. A* **1977**, *81*, 1498−1501.
(43) Shkrob, I. A. The structure of the hydrated electron. Part 1. Magnetic resonance of internally trapping water anions: A density functional theory study. *J. Phys. Chem. A* **2007**, *111*, 5223−5231.
(44) Bales, B. L.; Helbert, J.; Kevan, L. Electron paramagnetic resonance and electron−nuclear double resonance line shape studies of trapped electrons in γ-irradiated deuterium-substituted 10 *M* sodium hydroxide alkaline ice glass. *J. Phys. Chem. A* **1974**, *78*, 221−231.
(45) Astashkin, A. V.; Dikanov, S. A.; Tsvetkov, Y. D. Hyperfine interactions of deuterium nuclei in the nearest surroundings of trapped electrons in alkaline glass. *Chem. Phys. Lett.* **1988**, *144*, 258−264.
(46) Avery, E. C.; Remko, J. R.; Smaller, B. EPR detection of the hydrated electron in liquid water. *J. Chem. Phys.* **1968**, *49*, 951.
(47) Ohno, K.; Takemura, I.; Sohma, J. Resolution enhanced ESR spectra of the trapped electrons in an alkaline glass. *J. Chem. Phys.* **1972**, *56*, 1202−1206.
(48) Fessenden, R. W.; Verma, N. C. Time resolved electron spin resonance spectroscopy. III. Electron spin resonance emission from the hydrated electron. Possible evidence for reaction to the triplet state. *J. Am. Chem. Soc.* **1976**, *98*, 243−244.
(49) Jeevarajan, A. S.; Fessenden, R. W. ESR studies of solvated electron in liquid solution using photolytic production. *J. Phys. Chem. A* **1989**, *93*, 3511−3514.
(50) Shiraishi, H.; Ishigure, K.; Morokuma, K. An ESR study on solvated electrons in water and alcohols: Difference in the *g* factor and related analysis of the electronic state by MO calculation. *J. Chem. Phys.* **1988**, *88*, 4637−4649.
(51) Veselov, A. V.; Fessenden, R. W. Medium effects on the ESR spectrum of the hydrated electron. *J. Phys. Chem. A* **1993**, *97*, 3497−3499.
(52) Hare, P. M.; Price, E. A.; Stanisky, C. M.; Janik, I.; Bartels, D. M. Solvated electron extinction coefficient and oscillator strength in high temperature water. *J. Phys. Chem. A* **2010**, *114*, 1766−1775.
(53) Shkrob, I. A.; Glover, W. J.; Larsen, R. E.; Schwartz, B. J. The structure of the hydrated electron. Part 2. A mixed quantum/classical molecular dynamics embedded cluster density functional theory theory: Single-excitation configuration interaction study. *J. Phys. Chem. A* **2007**, *111*, 5232−5243.
(54) Borrelli, W. R.; Liu, X.; Schwartz, B. J. How the choice of exchange-correlation functional affects DFT-based simulations of the hydrated electron. *J. Chem. Phys.* **2025**, *162*, No. 110901.
(55) Johnson, E. R.; Otero-de-la-Roza, A.; Dale, S. G. Extreme density-driven delocalization error for a model solvated-electron system. *J. Chem. Phys.* **2013**, *139*, No. 184116.
(56) Narvaez, W. A.; Bartels, D. M.; Thompson, W. H. Assessing the limitations of self-interaction-corrected functionals for describing the hydrated electron. *J. Chem. Theory Comput.* **2026**, *22*, 5473−5483.
(57) Miceli, G.; de Gironcoli, S.; Pasquarello, A. Isobaric first-principles molecular dynamics of liquid water with nonlocal van der Waals interactions. *J. Chem. Phys.* **2015**, *142*, No. 034501.
(58) Chen, W.; Ambrosio, F.; Miceli, G.; Pasquarello, A. *Ab initio* electronic structure of liquid water. *Phys. Rev. Lett.* **2016**, *117*, No. 186401.
(59) Ambrosio, F.; Miceli, G.; Pasquarello, A. Structural, dynamical, and electronic properties of liquid water: A hybrid functional study. *J. Phys. Chem. B* **2016**, *120*, 7456−7470.
(60) Ambrosio, F.; Pasquarello, A. Reactivity and energy level of a localized hole in liquid water. *Phys. Chem. Chem. Phys.* **2018**, *20*, 30281−30289.
(61) Lan, J.; Chergui, M.; Pasquarello, A. Dynamics of the charge transfer to solvent process in aqueous iodide. *Nat. Commun.* **2024**, *15*, No. 2544.
(62) Ambrosio, F.; Chen, W.; Pasquarello, A. Electronic energy levels of aqueous hydroxyl species. *Phys. Chem. Chem. Phys.* **2025**, *27*, 23079−23090.
(63) Goedecker, S.; Teter, M.; Hutter, J. Separable dual-space Gaussian pseudopotentials. *Phys. Rev. B* **1996**, *54*, No. 1703.
(64) Hartwigsen, C.; Goedecker, S.; Hutter, J. Relativistic separable dual-space gaussian pseudopotentials from H to Rn. *Phys. Rev. B* **1998**, *58*, No. 3641.
(65) Krack, M. Pseudopotentials for H to Kr optimized for gradient-corrected exchange-correlation functionals. *Theor. Chem. Acc.* **2005**, *114*, 145−152.
(66) Perdew, J. P.; Burke, K.; Ernzerhof, M. Generalized gradient approximations made simple. *Phys. Rev. Lett.* **1996**, *77*, No. 3865.
(67) Sabatini, R.; Gorni, T.; de Gironcoli, S. Nonlocal van der Waals density functional made simple and efficient. *Phys. Rev. B* **2013**, *87*, No. 041108(R).
(68) Vydrov, O. A.; Van Voorhis, T. Nonlocal van der Waals density functional: The simpler the better. *J. Chem. Phys.* **2010**, *133*, No. 244103.
(69) Bernas, A.; Ferradini, C.; Jay-Gerin, J.-P. On the electronic structure of liquid water: Facts and reflections. *Chem. Phys.* **1997**, *222*, 151−160.
(70) Coe, J. V.; Earhart, A. D.; Cohen, M. H.; Hoffman, G. J.; Sarkas, H. W.; Bowen, K. H. Using cluster studies to approach the electronic structure of bulk water: Reassessing the vacuum level, conduction band edge, and band gap of water. *J. Chem. Phys.* **1997**, *107*, 6023−6031.
(71) Fang, C.; Li, W.-F.; Koster, R. S.; Klimes, J.; van Blaaderen, A.; van Huis, M. A. The accurate calculation of the band gap of liquid water by means of *GW* corrections applied to plane-wave density functional theory molecular dynamics simulations. *Phys. Chem. Chem. Phys.* **2015**, *17*, 365−375.
(72) Adriaanse, C.; Cheng, J.; Chau, V.; Sulpizi, M.; VandeVondele, J.; Sprik, M. Aqueous redox chemistry and the electronic band structure of liquid water. *J. Phys. Chem. Lett.* **2012**, *3*, 3411−3415.
(73) Cheng, J.; Sprik, M. Alignment of electronic energy levels at electrochemical interfaces. *Phys. Chem. Chem. Phys.* **2012**, *14*, 11245−11267.
(74) Ambrosio, F.; Miceli, G.; Pasquarello, A. Redox levels in aqueous solution: Effect of van der Waals interactions and hybrid functionals. *J. Chem. Phys.* **2015**, *143*, No. 244508.
(75) Zhang, C.; Tang, F.; Chen, M.; Xu, J.; Zhang, L.; Qiu, D. Y.; Perdew, J. P.; Klein, M. L.; Wu, X. Modeling liquid water by climbing up Jacob's ladder in density functional theory facilitated by using deep neural network potentials. *J. Phys. Chem. B* **2021**, *125*, 11444−11456.
(76) Gray, M.; Mandal, A.; Herbert, J. M. Revisiting the half-and-half functional. *J. Phys. Chem. A* **2025**, *129*, 3969−3982.
(77) Soper, A. K.; Bruni, F.; Ricci, M. A. Site-site pair correlation functions of water from 25 to 400 °C: Revised analysis of new and old diffraction data. *J. Chem. Phys.* **1997**, *106*, 247−254.
(78) Kühne, T. D.; Iannuzzi, M.; Del Ben, M.; et al. CP2K: An electronic structure and molecular dynamics software package—Quickstep: Efficient and accurate electronic structure calculations. *J. Chem. Phys.* **2020**, *152*, No. 194103.
(79) Bussi, G.; Donadio, D.; Parrinello, M. Canonical sampling through velocity rescaling. *J. Chem. Phys.* **2007**, *126*, No. 014101.
(80) Nose, S. A unified formulation of the constant temperature molecular dynamics method. *J. Chem. Phys.* **1984**, *81*, 511−519.
(81) Brehm, M.; Thomas, M.; Gehrke, S.; Kircher, B. TRAVIS—A free analyzer for trajectories from molecular simulation. *J. Chem. Phys.* **2020**, *152*, No. 164105.
(82) Harvey, A. H. *Thermodynamic Properties of Water: Tabulation from the IAPWS Formulation for the Thermodynamic Properties of Ordinary Water Substance for General and Scientific Use*, Technical Report NISTIR 5078, 1995; National Institute of Standards and Technology, 1995.
(83) Berghold, G.; Mundy, C. J.; Romero, A. H.; Hutter, J.; Parrinello, M. General and efficient algorithms for obtaining

maximally localized Wannier functions. *Phys. Rev. B* **2000**, *61*, 10040−10048.
(84) Jacobson, L. D.; Herbert, J. M. Polarization-bound quasi-continuum states are responsible for the "blue tail" in the optical absorption spectrum of the aqueous electron. *J. Am. Chem. Soc.* **2010**, *132*, 10000−10002.
(85) Herbert, J. M.; Jacobson, L. D. Structure of the aqueous electron: Assessment of one-electron pseudopotential models in comparison to experimental data and time-dependent density functional theory. *J. Phys. Chem. A* **2011**, *115*, 14470−14483.
(86) Neese, F. Software update: The ORCA program system−version 6.0. *WIREs Comput. Mol. Sci.* **2025**, *15*, No. e70019.
(87) Herbert, J. M.; Head-Gordon, M. Calculation of electron detachment energies for water cluster anions: An appraisal of electronic structure methods, with application to $(H_2O)_{20}^-$ and $(H_2O)_{24}^-$. *J. Phys. Chem. A* **2005**, *109*, 5217−5229.
(88) Nagy, B.; Jensen, F. Basis Sets in Quantum Chemistry. In *Reviews in Computational Chemistry*; Parrill, A. L.; Lipkowitz, K. B., Eds.; Wiley, 2017; Vol. *30*, Chapter 3; pp 93−149.
(89) Becke, A. D. A multicenter numerical integration scheme for polyatomic molecules. *J. Chem. Phys.* **1988**, *88*, 2547−2553.
(90) Herbert, J. M.; Carter-Fenk, K. Electrostatics, charge transfer, and the nature of the halide-water hydrogen bond. *J. Phys. Chem. A* **2021**, *125*, 1243−1256.
(91) Bowling, P. E.; Gray, M.; Paul, S. K.; Herbert, J. M. Testing a heterogeneous polarizable continuum model against exact Poisson boundary conditions. *J. Chem. Theory Comput.* **2025**, *21*, 1722−1738.
(92) Murray, C. W.; Handy, N. C.; Laming, G. J. Quadrature schemes for integrals of density functional theory. *Mol. Phys.* **1993**, *78*, 997−1014.
(93) Dasgupta, S.; Herbert, J. M. Standard grids for high-precision integration of modern density functionals: SG-2 and SG-3. *J. Comput. Chem.* **2017**, *38*, 869−882.
(94) Epifanovsky, E.; Gilbert, A. T. B.; Feng, X.; et al. Software for the frontiers of quantum chemistry: An overview of developments in the Q-Chem 5 package. *J. Chem. Phys.* **2021**, *155*, No. 084801.
(95) Cheng, B.; Engel, E. A.; Behler, J.; Dellago, C.; Ceriotti, M. Ab initio thermodynamics of liquid and solid water. *Proc. Natl. Acad. Sci. U.S.A.* **2019**, *116*, 1110−1115.
(96) Reinhardt, A.; Cheng, B. Quantum-mechanical exploration of the phase diagram of water. *Nat. Commun.* **2021**, *12*, No. 588.
(97) Villard, J.; Bircher, M. P.; Rothlisberger, U. Structure and dynamics of liquid water from *ab initio* simulations: Adding Minnesota density functionals to Jacob's ladder. *Chem. Sci.* **2024**, *15*, 4434−4451.
(98) Shank, A.; Wang, Y.; Kaledin, A.; Braams, B. J.; Bowman, J. M. Accurate *ab initio* and "hybrid" potential energy surfaces, intramolecular vibrational energies, and classical IR spectrum of the water dimer. *J. Chem. Phys.* **2009**, *130*, No. 144314.
(99) Rocher-Casterline, B. E.; Ch'ng, L. C.; Mollner, A. K.; Reisler, H. Communication: Determination of the bond dissociation energy (D_0) of the water dimer, $(H_2O)_2$, by velocity map imaging. *J. Chem. Phys.* **2011**, *134*, No. 211101.
(100) Herbert, J. M.; Paul, S. K. Interaction energy analysis of monovalent inorganic anions in bulk water versus air/water interface. *Molecules* **2021**, *26*, No. 6719.
(101) Grossfield, A.; Ren, P.; Ponder, J. W. Ion solvation thermodynamics from simulation with a polarizable force field. *J. Am. Chem. Soc.* **2003**, *125*, 15671−15682.
(102) Paul, S. K.; Herbert, J. M. Probing interfacial effects on ionization energies: The surprising banality of anion−water hydrogen bonding at the air/water interface. *J. Am. Chem. Soc.* **2021**, *143*, 10189−10202.
(103) Golden, S.; Tuttle, T. R., Jr. Nature of solvated electron absorption spectra. *J. Chem. Soc., Faraday Trans. 2* **1979**, *75*, 474−484.
(104) Bartels, D. M.; Takahashi, K.; Cline, J. A.; Marin, T. W.; Jonah, C. D. Pulse radiolysis of supercritical water. 3. Spectrum and thermodynamics of the hydrated electron. *J. Phys. Chem. A* **2005**, *109*, 1299−1307.
(105) Du, Y.; Price, E.; Bartels, D. M. Solvated electron spectrum in supercooled water and ice. *Chem. Phys. Lett.* **2007**, *438*, 234−237.
(106) Coe, J. V.; Williams, S. M.; Bowen, K. H. Photoelectron spectra of hydrated electron clusters vs. cluster size. *Int. Rev. Phys. Chem.* **2008**, *27*, 27−51.
(107) Carmichael, I. Spectral moments of solvated electrons. *Chem. Phys. Lett.* **1978**, *56*, 339−342.
(108) Tuttle, T. R., Jr.; Golden, S. Solvated electrons: What is solvated? *J. Phys. Chem. A* **1991**, *95*, 5725−5736.
(109) Bartels, D. M. Moment analysis of hydrated electron cluster spectra: Surface or internal states? *J. Chem. Phys.* **2001**, *115*, 4404−4405.
(110) Hertwig, A.; Hippler, H.; Unterreiner, A.-N. Transient spectra, formation, and geminate recombination of solvated electrons in pure water UV-photolysis: An alternative view. *Phys. Chem. Chem. Phys.* **1999**, *1*, 5633−5642.
(111) Herbert, J. M. Density-Functional Theory for Electronic Excited States. In *Theoretical and Computational Photochemistry: Fundamentals, Methods, Applications and Synergy with Experimental Approaches*; García-Iriepa, C.; Marazzi, M., Eds.; Elsevier: Amsterdam, 2023, Cpahter 3; pp 69−118.
(112) Baer, R.; Livshits, E.; Salzner, U. Tuned range-separated hybrids in density functional theory. *Annu. Rev. Phys. Chem.* **2010**, *61*, 85−109.
(113) Mandal, A.; Herbert, J. M. Simplified tuning of long-range corrected time-dependent density functional theory. *J. Phys. Chem. Lett.* **2025**, *16*, 2672−2680.
(114) Rohrdanz, M. A.; Martins, K. M.; Herbert, J. M. A long-range-corrected density functional that performs well for both ground-state properties and time-dependent density functional theory excitation energies, including charge-transfer excited states. *J. Chem. Phys.* **2009**, *130*, No. 054112.
(115) Tauber, M. J.; Mathies, R. A. Structure of the aqueous solvated electron from resonance Raman spectroscopy: Lessons from isotopic mixtures. *J. Am. Chem. Soc.* **2003**, *125*, 1394−1402.
(116) Borrelli, W. R.; Liu, X.; Schwartz, B. J. The solvation entropy of different simulation models of the hydrated electron. *J. Phys. Chem. Lett.* **2026**, *17*, 1899−1906.
(117) Tran, V. A.; Neese, F. Double-hybrid density functional theory for g-tensor calculations using gauge including atomic orbitals. *J. Chem. Phys.* **2020**, *153*, No. 054105.
(118) Rana, B.; Herbert, J. M. Role of hemibonding in the structure and ultraviolet spectroscopy of the aqueous hydroxyl radical. *Phys. Chem. Chem. Phys.* **2020**, *22*, 27829−27844.
(119) Rana, B.; Herbert, J. M. Hidden hemibonding in the aqueous hydroxyl radical. *J. Phys. Chem. Lett.* **2021**, *12*, 8053−8060.
(120) Herbert, J. M.; Head-Gordon, M. Charge penetration and the origin of large O−H vibrational red-shifts in hydrated-electron clusters, $(H_2O)_n^-$. *J. Am. Chem. Soc.* **2006**, *128*, 13932−13939.
(121) Rassolov, V. A.; Chipman, D. M. New operators for electronic density calculations. I. Derivations and formal analysis. *J. Chem. Phys.* **1996**, *105*, 1470−1478.
(122) Rassolov, V. A.; Chipman, D. M. New operators for electronic density calculations. II. Applications to hydrogen, first-row atoms, and first-row diatomic hydrides. *J. Chem. Phys.* **1996**, *105*, 1479−1491.
(123) Wang, B.; Baker, J.; Pulay, P. Density functional implementation of a Gaussian-weighted operator for spin densities. *Phys. Chem. Chem. Phys.* **2000**, *2*, 2131−2135.
(124) Nicolas, C.; Boutin, A.; Levy, B.; Borgis, D. Molecular simulation of a hydrated electron at different thermodynamic state points. *J. Chem. Phys.* **2003**, *118*, 9689−9696.
(125) Boutin, A.; Spezia, R.; Coudert, F.-X.; Mostafavi, M. Molecular dynamics simulations of the temperature and density dependence of the absorption spectra of hydrated electron and solvated silver atom in water. *Chem. Phys. Lett.* **2005**, *409*, 219−223.

https://doi.org/10.1021/jacs.6c07020
J. Am. Chem. Soc. 2026, 148, 36675−36686

(126) Flanagin, L. W.; Balbuena, P. B.; Johnston, K. P.; Rossky, P. J. Ion solvation in supercritical water based on an adsorption analogy. *J. Phys. Chem. B* **1997**, *101*, 7998−8005.
(127) Guàrdia, E.; Martí, J.; Padró, J. A. Ion solvation in aqueous supercritical electrolyte solutions at finite concentrations: a computer simulation study. *Theor. Chem. Acc.* **2006**, *115*, 161−169.
(128) Ma, H. Hydration structure of Na^+, K^+, F^-, and Cl^- in ambient and supercritical water: A quantum mechanics/molecular mechanics study. *Int. J. Quantum Chem.* **2014**, *114*, 1006−1011.
(129) Tucker, S. C.; Maddox, M. W. The effect of solvent density inhomogeneities on solute dynamics in supercritical fluids: A theoretical perspective. *J. Phys. Chem. B* **1998**, *102*, 2437−2453.
(130) Tucker, S. C. Solvent density inhomogeneities in supercritical fluids. *Chem. Rev.* **1999**, *99*, 391−418.
(131) Ohio Supercomputer Center 2026 http://osc.edu/ark:/19495/f5s1ph73. (accessed July 30, 2026).

https://doi.org/10.1021/jacs.6c07020
J. Am. Chem. Soc. 2026, 148, 36675−36686